

THE SENSITIVITY OF FIRST GENERATION EPOCH OF REIONIZATION OBSERVATORIES AND THEIR POTENTIAL FOR DIFFERENTIATING THEORETICAL POWER SPECTRA

JUDD D. BOWMAN^{1,2}, MIGUEL F. MORALES¹, JACQUELINE N. HEWITT^{1,2}

Draft version November 30, 2018

ABSTRACT

Statistical observations of the epoch of reionization (EOR) power spectrum provide a rich data set for understanding the transition from the cosmic “dark ages” to the ionized universe we see today. EOR observations have become an active area of experimental cosmology, and three first generation observatories—MWA, PAST, and LOFAR—are currently under development. In this paper we provide the first quantitative calculation of the three dimensional power spectrum sensitivity, incorporating the design parameters of a planned array. This calculation is then used to explore the constraints these first generation observations can place on the EOR power spectrum. The results demonstrate the potential of upcoming power spectrum observations to constrain theories of structure formation and reionization.

Subject headings: Cosmology: Early Universe, Galaxies: Intergalactic Medium, Radio Lines: General, Techniques: Interferometric

1. INTRODUCTION

The reionization history of the universe provides an important tool for understanding the epoch of structure formation and the appearance of the first luminous objects. Existing experimental clues about this period are confusing, however. The large Thompson scattering measured by the WMAP satellite implies that reionization occurred by redshift $z \approx 15$ (Kogut et al. 2003), whereas quasar absorption line studies show significant neutral hydrogen at redshift $z \approx 6$ (Djorgovski et al. 2001; Becker et al. 2001; Fan et al. 2003; Wyithe & Loeb 2004b). Reconciling these measurements seems to require a fairly complicated reionization history (Haiman & Holder 2003; Cen 2003; Sokasian et al. 2003; Madau et al. 2004).

Directly observing the process of structure formation during the epoch of reionization (EOR) would resolve these uncertainties. As the primordial hydrogen cools and later reheats, density contrasts are revealed as fluctuations in the brightness temperature of the redshifted 21 cm neutral hydrogen line (Sunyaev & Zeldovich 1972; Hogan & Rees 1979; Scott & Rees 1990; Shapiro et al. 1994; Loeb & Zaldarriaga 2004; Barkana & Loeb 2005b). Additionally, as the first luminous objects ionize their surroundings bubbles appear in the diffuse 21 cm emission (Madau et al. 1997; Tozzi et al. 2000; Ciardi & Madau 2003; Zaldarriaga et al. 2004; Furlanetto et al. 2004a).

The neutral hydrogen emission from this period appears in the low radio frequencies as faint fluctuations between 75 → 200 MHz (for redshifts 18 → 6). Directly imaging the fluctuations will require the sensitivity of the Square Kilometer Array (Furlanetto & Briggs 2004), but statistical observations of the fluctuation power spectrum should be obtainable with the much smaller first generation EOR observatories currently under construction. Measuring the power spectrum and its evolution would provide a wealth of information about structure formation and the fundamental astrophysics behind reionization. At high redshift, observations would ex-

plore structure formation in the linear gravity regime and constrain the properties of dark matter (Loeb & Zaldarriaga 2004; Pen 2004), and at lower redshifts they would probe reionization and follow the emergence and properties of the first luminous objects (Tozzi et al. 2000; Somerville et al. 2003; Furlanetto et al. 2004a,b; Iliev et al. 2005).

Measuring the EOR power spectrum builds on the statistical techniques developed for analyzing the cosmic microwave background (CMB) anisotropy. Unlike the CMB, however, the EOR signal is fully three-dimensional since the frequency of the redshifted 21 cm line maps to the line-of-sight distance. Recent efforts have shown how the three-dimensional nature of the EOR signal can be used to increase instrumental sensitivity and mitigate against foreground contamination (Morales & Hewitt 2004; Zaldarriaga et al. 2004; Bharadwaj & Ali 2005).

In this paper, we utilize the formalism of Morales & Hewitt (2004) and Morales (2005) with the parameters of a planned array to provide the first quantitative calculation of the three dimensional power spectrum sensitivity of forthcoming observations. The calculations include realistic observational parameters such as antenna layout, field of view, and antenna temperature, and provide a fiducial mark for the capabilities of the first generation EOR observations.

We begin in Section 2 by detailing the observational parameters and techniques used for our calculation. Section 3 then presents the results, analyzing the EOR sensitivity as a function of length scale, redshift, and global ionization fraction. We conclude in Section 4 with a discussion of the additional experimental issues which must be confronted in a realistic array.

2. FIRST GENERATION EOR EXPERIMENTS

The first generation of radio observatories targeting the EOR power spectrum consists of three instruments that are currently under development and should be operational by the end of the decade. The instruments are PAST, MWA, and LOFAR.

The Primeval Structure Telescope (PAST) is a project of the National Astronomical Observatories, Chinese Academy of Sciences. PAST is located in the radio quiet Ulaistai valley in northwestern China, and will consist of 10,000 single-

Electronic address: jdbowman@mit.edu; mmorales@space.mit.edu; jhewitt@space.mit.edu

¹ MIT Kavli Institute for Astrophysics and Space Research, 77 Massachusetts Ave., Cambridge, MA 02139

² MIT Department of Physics



FIG. 1.— This photograph shows the first MWA prototype antenna being tested on site in Mileura. The antenna consists of 16 crossed-dipoles in a four-by-four meter grid and is elevated approximately 0.5 m above the ground. Five hundred antennas will be placed in a 1500 m diameter array for the low frequency band of the first-generation MWA.

polarization yagis observing the north celestial pole. PAST will be the first EOR array to begin acquiring data. (Pen et al. 2005, submitted)

The Mileura Wide-field Array (MWA) is a collaboration of the Massachusetts Institute of Technology, Harvard-Smithsonian Center for Astrophysics, the Australian University Consortium, the Australian National Telescope Facility, and the Western Australian government. The MWA will be located at the Mileura radio quiet site in the Western Australian desert. The low frequency portion of the array will consist of 8,000 dual-polarization dipoles and feature very high spatial dynamic range and calibration precision, including polarization. (Salah et al. 2005, in press)

The Low Frequency Array (LOFAR) is being built by ASTRON in the Netherlands, and will consist of 72,000 dual polarization dipoles operating at EOR frequencies. While the radio interference environment of the Netherlands is challenging, LOFAR will have by far the largest collecting area of the first generation EOR arrays. (Kassim et al. 2004)

2.1. The Fiducial Observation

To calculate accurately the sensitivity of an EOR measurement, we need to specify both the details of the instrument and the observing strategy. For this paper we wish to choose a set of realistic observation parameters so that we can discuss the statistical sensitivity of first-generation EOR experiments.

We have chosen our reference measurement to be a deep observation of a single target field using an array configuration based on the MWA. Of the first generation arrays, the MWA is intermediate in theoretical sensitivity and has good control of systematic errors.

Many factors contribute to the instrumental response of an array. Among the most important to consider are the field of view, angular resolution, collecting area, antenna distribution, and bandwidth.

For the MWA, each antenna consists of 16 crossed-dipoles in a four-by-four meter grid as shown in Figure 1. A beam-forming operation on the dipoles within an antenna produces a field of view of $15\text{--}45^\circ$ (FWHM), depending on frequency.

The reference array consists of $N = 500$ antennas distributed within a $D = 1500$ m diameter circle. The density of antennas as a function of radius is taken to be approximately $\rho(r) \sim r^{-2}$. The angular resolution is given by λ/D and the collecting area by $N dA$, where dA is the collecting area of each antenna and scales like $dA \sim 16(\lambda^2/4)$ for wavelengths below two meters.

Although the bandwidth of the MWA is 32 MHz, we re-

TABLE 1
FIDUCIAL OBSERVATION PARAMETERS

Parameter	Value
Array configuration, $\rho(r)$	$\sim r^{-2}$
Array diameter, D	1500 m
Bandwidth, B	8 MHz
Frequency resolution	8 kHz
Integration time, t	360 hours
Number of antennas, N	500

NOTE. — Observation parameters used in the sensitivity analysis.

TABLE 2
REDSHIFT DEPENDENT PARAMETERS

	$z = 6$	$z = 8$	$z = 10$	$z = 12$
Angular resolution ($^\circ$)	0.06	0.07	0.09	0.10
Antenna collecting area, dA (m^2)	9	14	18	18
Antenna response scale, Θ ($^\circ$)	19	31	38	43
Frequency (MHz)	203	158	129	109
System temperature, T_{sys} (K)	250	440	690	1000

NOTE. — Characteristics of the fiducial observation that depend on frequency, and thus on redshift. Note that the antenna collecting area is capped above $z = 10$ due to self-shadowing by the antennas at low frequencies. Also, the system temperature is dominated by sky noise and depends significantly on frequency.

strict the bandwidth of our reference observation to $B = 8$ MHz. This avoids complications introduced by cosmic evolution, yet still provides measurements along the line-of-sight at the length scales of the strongest fluctuations in the 21 cm signal. It is also the minimum bandwidth suggested by Wyithe & Loeb (2004a) to ensure sensitivity to fluctuations during the final stage of reionization when ionized bubbles first overlap completely.

Finally, the integration time on the target field must also be specified. Observing for four hours per day over the course of a six month season would result in approximately 720 hours of integration. Conservatively rejecting half the data for non-ideal conditions yields 360 hours of integration during the most favorable circumstances.

The full parameter set for our fiducial observation is summarized in Tables 1 and 2.

2.2. The Data Cylinder

Since neutral hydrogen is optically thin to the 21 cm line, the visibility measurements of EOR observatories inherently sample the emission from a three dimensional volume of space at high redshift. To good approximation, these measurements form a three dimensional data cylinder in visibility space (u, v, f) due to the overall circular shape of the array.

By applying Fourier transforms along one or more of the coordinates of the data cylinder, the measurements also may be represented as cylinders in several additional useful coordinate spaces. These include real space (with units of comoving Mpc), cosmological Fourier space ($\mathbf{k} \equiv k_1, k_2, k_3$), image space (θ_x, θ_y, f) , and instrumental Fourier space (u, v, η) . Each coordinate space possesses advantages for different stages of the analysis. For example, point source foreground removal is most conveniently accomplished in the image space, while the power spectrum of the EOR signal has symmetries that are most easily exploited in the Fourier space. Since space is isotropic (rotationally invariant) the EOR signal is approx-

TABLE 3
DATA CYLINDER DIMENSIONS FOR REDSHIFT $z = 8$

Frame	Diameter	Depth (Line-of-sight)
Cosmological Fourier (\mathbf{k})	0.55 Mpc^{-1}	48 Mpc^{-1}
Image (θ_x, θ_y, f)	62°	8 MHz
Instrumental Fourier (u, v, η)	790λ	$1.2 \cdot 10^{-4} \text{ Hz}^{-1}$
Real	2400 Mpc	130 Mpc
Visibility (u, v, f)	790λ	8 MHz

NOTE. — Dimensions of the data cylinder at redshift $z = 8$ for the example array configuration in different frames. The diameter of the cylinder is in the plane of the first two coordinates and the depth is along the third coordinate.

imately spherically symmetric in the Fourier space. All of the measurements from a spherical shell are thus drawn from the same statistical ensemble and can be averaged together to maximize the signal to noise (Morales & Hewitt 2004; Morales 2005). The spherical symmetry is the basis of the three dimensional statistical EOR measurement and employed in our sensitivity calculation below.

At redshift $z = 8$, the data cylinder in cosmological Fourier space has a diameter of 0.55 Mpc^{-1} in the $k_1 k_2$ -plane and spans 48 Mpc^{-1} in the line-of-sight direction. Clearly the data cylinder is very elongated in Fourier space, with the line-of-sight axis responsible for the high spatial frequency contribution. Table 3 lists the dimensions of the data cylinder in additional frames. We will see in the following sections that the dimensions of the data cylinder play an important role in the planned statistical measurements.

2.3. The Instrumental Response

We have so far outlined the details of the fiducial observation. In order to understand the sensitivity of the experiment, the 21 cm power spectrum must be mapped to an instrumental response. Following the development of Morales & Hewitt (2004), this response is given by the convolution of the power spectrum, $P(\mathbf{k})$, with the instrumental window function, $W(\mathbf{k})$, according to

$$C'(\mathbf{k}) = \langle |\Delta I(\mathbf{k})|^2 \rangle = \int P(\mathbf{k}) |W(\mathbf{k} - \mathbf{k}')|^2 d^3 k'. \quad (1)$$

The window function is given by the array's spatial and frequency response. We approximate it with a function that is independent of frequency within the band and that depends on θ as

$$W(\theta) = \cos^2\left(\frac{\pi\theta}{\Theta}\right), \quad \theta < \Theta \quad (2)$$

where Θ is the antenna response scale size and $W(\theta)$ is zero outside the defined region. In general the Fourier space window function, $W(\mathbf{k})$, is a very sharply peaked function. At redshift $z = 8$, the width of $W(\mathbf{k})$ for the example array configuration is approximately 0.003 Mpc^{-1} in the $k_1 k_2$ -plane and 0.05 Mpc^{-1} along the k_3 -direction.

Inherent in every radio observation is thermal noise. The contribution of this noise can be estimated by dividing the Fourier space into a large number of independent cells, where the size of each cell is given by the window function, $W(\mathbf{k})$. The thermal noise per independent cell can then be approximated using (Morales 2005, His Equation 11)

$$[C_{ij}^N(\mathbf{u})]_{\text{rms}} = 2 \left(\frac{2k_B T_{\text{sys}}}{\epsilon dA d\eta} \right)^2 \frac{1}{B \bar{n}(\mathbf{u}) t} \delta_{ij}, \quad (3)$$

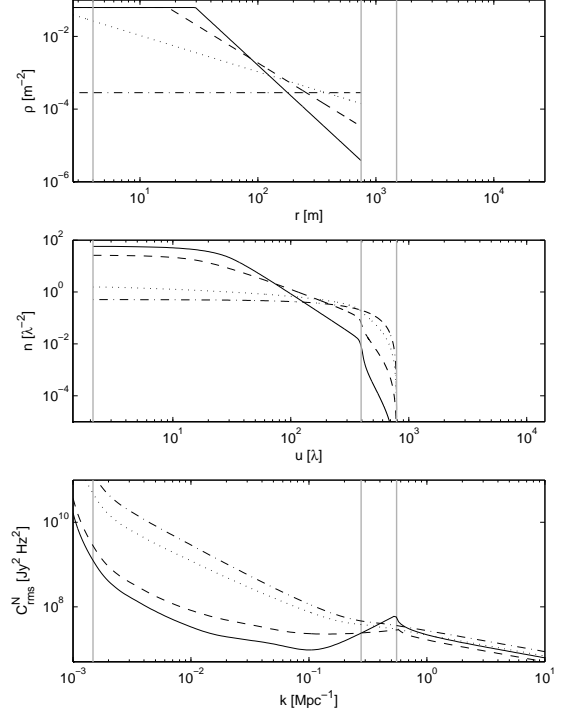


FIG. 2.— Four model antenna configurations (top), the corresponding densities of visibility measurements (middle), and $1\text{-}\sigma$ uncertainties in the measured power spectrum due to thermal noise (bottom). The antenna configurations are characterized by power-law density profiles, $\rho(r) \sim r^{-3}$ (solid), r^{-2} (dash), r^{-1} (dot), and r^0 (dash-dot). The abscissas of the three panels are aligned so that the r , u , and k coordinates correspond. The vertical gray bars represent the 4 m width of an antenna (far left), the 750 m radius of the array (middle) and the 1500 m maximum baseline in the uv -plane (right). The uncertainties in the bottom panel extend beyond the bounds of the maximum baseline due to the elongated k_3 axis, as described in Section 2.2

where dA is the physical antenna area, $d\eta$ is the inverse of the total bandwidth, k_B is Boltzmann's constant, T_{sys} is the total system temperature, ϵ is the efficiency, B is the total bandwidth, \bar{n} is the time average number of baselines in an observing cell, $\mathbf{u} \equiv \sqrt{u^2 + v^2}$, and t is the total observation time.

The thermal noise is approximately independent of frequency within the observing band and has a cylindrical symmetry in Fourier space. The measured value of the power spectrum, however, is an average over spherical shells in Fourier space. Thus, to calculate the uncertainty due to thermal noise in the measurement, we must average the uncertainty contributions from all of the independent cells in spherical shells. The result is that the uncertainty at a given length scale has a somewhat complicated dependence on thermal noise, and therefore, on the antenna distribution of the array.

The top panel of Figure 2 shows four candidate antenna profiles for the MWA. All of the distributions contain 500 antennas and respect the minimum physically possible antenna spacing (which is responsible for the density plateaus as $r \rightarrow 0$). The four distributions are labelled by the antenna density profiles at large radii: $\rho(r) \sim r^0$, r^{-1} , r^{-2} , and r^{-3} .

The second panel shows the density of visibility measurements in the uv -plane for each of the antenna distributions. The density is related to the average number of measurements per cell, $\bar{n}(\mathbf{u})$, in Equation 3 by the cell size.

The third panel of Figure 2 gives the uncertainty due to thermal noise per spherical logarithmic shell in cosmological

Fourier space with five bins per decade. Two limiting regimes are evident in this plot. For small shells in Fourier space, the noise depends strongly on the density profile since only visibility measurements from baselines smaller than a shell's radius contribute. Increasing the steepness of the antenna profile condenses the visibility measurements toward the origin of the $k_1 k_2$ -plane, reducing the noise in small shells. In the other limiting case, shells in Fourier space that have extended beyond the radius of the largest baseline in the $k_1 k_2$ -plane ($k \gtrsim 0.5 \text{ Mpc}^{-1}$) include information from every antenna, and the density profile has little effect on the noise.

Second order effects such as the distinction between coherent integration of visibility measurements within a cell and the incoherent averaging of independent cells leads to the small differences seen at large k . Between these limiting cases, the interaction of the cylindrical symmetry of the thermal noise with the spherical symmetry and logarithmic widths of the shells causes a more complicated behavior. At length scales comparable to the diameter of the data cylinder, where visibility measurements are sparse over much of a shell, the uncertainty even has a local maximum for the centrally condensed arrays.

It is clear from Figure 2 that the sensitivity of the statistical EOR measurement is tightly linked to the array antenna distribution. The difference in uncertainty between the uniform distribution and the steeper power-law distributions is as much as two orders of magnitude, depending on the length scale of interest. As indicated in Table 1, we will use the $\rho(r) \sim r^{-2}$ antenna distribution as our reference in the remainder of the paper.

2.4. The Model Power Spectrum

For our calculations we use a simple model of the redshifted 21 cm power spectrum that has been used commonly in the literature, in which the hydrogen in the intergalactic medium (IGM) is fully neutral, follows the dark matter distribution, and has a spin temperature much larger than the CMB temperature (Madau et al. 1997; Tozzi et al. 2000; Zaldarriaga et al. 2004). This is a reasonable model for the fluctuations after the spin temperature has been heated by the Wouthuysen-Field effect or other processes and before reionization by the first luminous objects, though over what redshift range this may be observed is uncertain.

This model power spectrum is computed using CMBFAST (Seljak & Zaldarriaga 1996) and does not include velocity distortions, but Barkana & Loeb (2005a) have shown that including peculiar velocities increases the signal amplitude by about a factor of two. Distortions due to geometrical effects (such as a scaling between the line-of-sight and sky-plane axes) and peculiar velocities could allow separation of cosmological and astrophysical effects and provide sensitive probes of the underlying cosmology, but are not included in our simple model (Alcock & Paczynski 1979; Kaiser 1987; Barkana & Loeb 2005a).

Figure 3 shows the results of performing the above calculations for the fiducial experiment using our simple neutral hydrogen power spectrum at redshift $z = 8$ with standard concordance cosmology ($\Omega_M = 0.3, \Omega_\Lambda = 0.7, h = 0.7$). The power spectrum was convolved with the instrumental window function to produce the solid black line, which is plotted in the observer units $\text{Jy}^2 \text{ Hz}^2$ (see Morales & Hewitt (2004) for a discussion of units).

Just as there is an inherent uncertainty due to thermal noise, there is also an inherent cosmic sample variance in the ob-

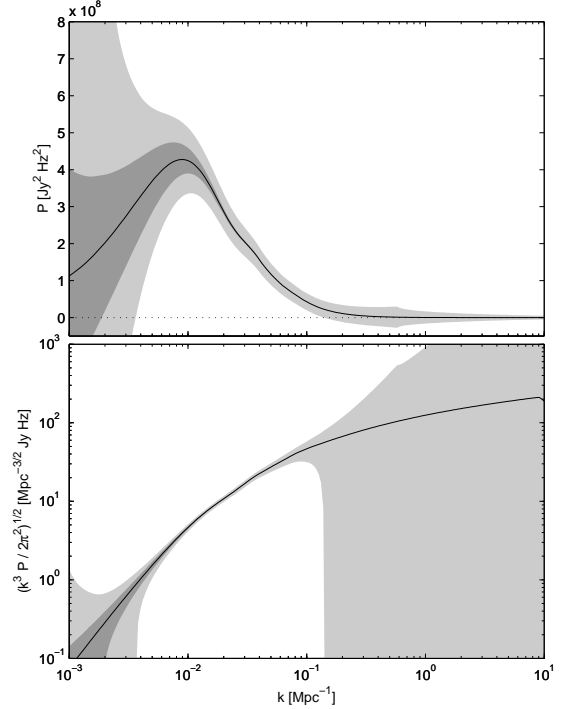


FIG. 3.— Combined 1- σ uncertainty for logarithmic shells of width $k^{0.2}$ (equivalent to five spectral points per decade) in the measured power spectrum due to sample variance (dark gray) and combined sample and thermal variance (light gray). The instrumental response to the ideal neutral hydrogen power spectrum at redshift $z = 8$ is shown in black. Logarithmic shells of width $k^{0.2}$ were used for bins. The details of the example observation configuration are specified in Tables 1 and 2. In the upper panel the signal is shown in observer units (where the measurement errors are Gaussian), while the lower panel uses the theoretical convention by changing the ordinate to $(k^3 P / 2\pi^2)^{1/2}$ and plotting on log-log axes.

served power spectrum. For a spherical shell in Fourier space, the sample variance can be estimated by considering the number of independent samples in the shell and approximating by using Gaussian statistics. This uncertainty is plotted as the dark gray region around the ideal power spectrum in Figure 3, while the combined uncertainty due to sample variance and thermal noise is added in quadrature, and the light gray region shows the full 1-sigma uncertainty.

3. RESULTS

3.1. The Measured Power Spectrum

Several effects of the instrumental response are contained in the measured power spectrum shown in Figure 3. Since the shape of the power spectrum is smeared by convolution with the instrumental window function, both the relative amplitude of the peak and the distinction of the baryon bump at $k \simeq 0.04$ are slightly reduced. In addition, the uncertainty due to thermal noise and cosmic sample variance increases rapidly as $k \rightarrow 0$, creating unfavorable sensitivity on large length scales.

The field of view is a significant factor determining the uncertainty at low k since the number of measurements at these scales is proportional to Θ^2 . Since the line-of-sight depth of the data cylinder in real space is less than these length scales, the advantages of a three-dimensional data set do not apply at low k . Only spherical shells with radius $k \gtrsim 0.02$ contain contributions from measurements with $k_3 \neq 0$.

The antenna distribution of the array, as we saw in Sec-

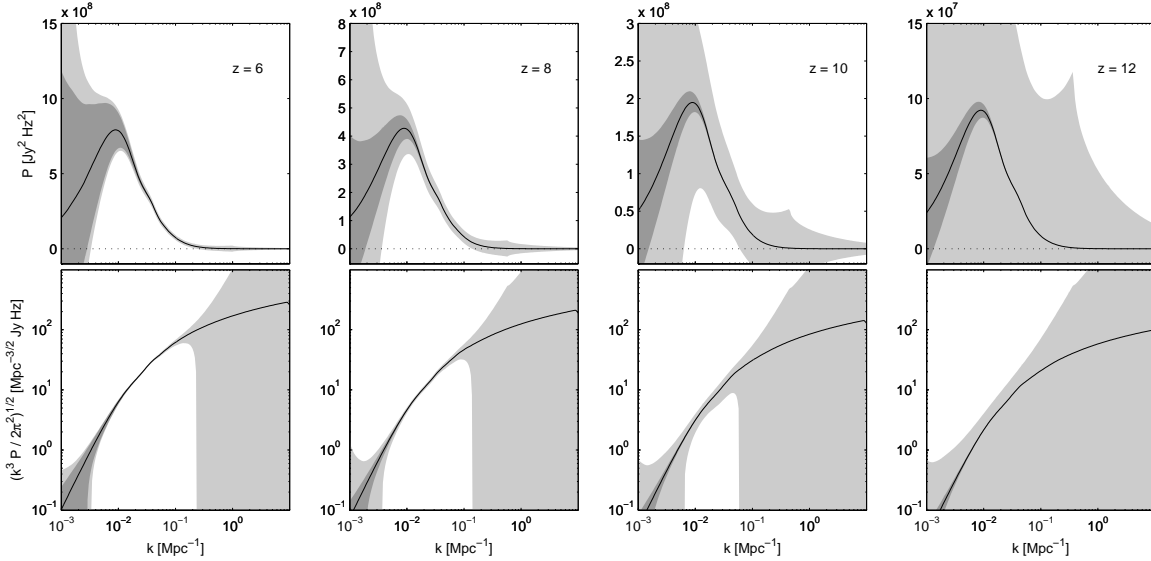


FIG. 4.— Same as Figure 3, but computed for observations at four redshifts. From left to right, the redshifts are $z = 6, 8, 10$, and 12 . Note that the vertical scales are different for each of the upper plots. The small peaks in uncertainty at $k \approx 0.5$ for $z = 10$ and 12 correspond to the increase in uncertainty due to thermal noise at length scales sampled by the largest baselines (see Figure 2).

tion 2, also affects the uncertainty of the measurement. Although more condensed arrays produced less uncertainty at large length scales (see Figure 2), other considerations which rely on synthesis imaging, such as removing astrophysical foregrounds, are adversely affected by condensing the antenna distribution and could potentially negate any benefits from such a change.

The sensitivity decreases again for large k since the power spectrum falls off more rapidly than the thermal noise. For the example array, the best range for constraining the measured power spectrum at redshift $z = 8$ is approximately $10^{-2} < k < 10^{-1} \text{ Mpc}^{-1}$.

3.2. Redshift Range

We can estimate the sensitivity of the array at additional redshifts by modifying the parameters of the fiducial observation. Four primary characteristics of the array are frequency dependent: the field of view (and thus the instrumental window function, W), the collecting area, the angular resolution, and the system temperature, T_{sys} . Table 2 lists the values of these parameters at four frequencies corresponding to redshifts of $z = 6, 8, 10$, and 12 .

The changes in these parameters require both the measurement uncertainty and the instrumental response to the redshifted 21 cm emission to be calculated for each redshift since the independent cell size, data cylinder dimensions, and characteristic thermal noise are directly affected. Figure 4 displays the results of such calculations for observations at the redshifts listed in Table 2. Again, the reference signal was a fully neutral IGM and the measurement was averaged over spherical logarithmic bins of width $k^{0.2}$.

The top panel, for redshift $z = 6$, illustrates the measurement with the greatest sensitivity. Two factors contribute to this performance: the amplitude of the power spectrum increases as $z \rightarrow 0$, and the system temperature of the instrument, primarily responsible for the uncertainty, decreases. On the other hand, the field of view and collecting area are reduced considerably, thus limiting the improvement in sensitivity for lower

redshifts. The net result is that the amplitude of the power spectrum increases by a factor of ~ 8 between redshifts $z = 12$ and 6 , while the system temperature, dominated by galactic foreground emission, decreases by a factor of ~ 3.5 . The sensitivity is sufficiently great at redshift $z = 6$ that the dominant source of uncertainty at large scales is sample variance. Although it is unlikely that no ionization will have occurred by redshift $z = 6$, even significantly weaker signals should be detectable.

There is a clear degradation of the measurement sensitivity in Figure 4 as the redshift increases until, by redshift $z = 12$, the observation is infeasible without longer integrations or additional collecting area.

3.3. Sensitivity to Reionization Models

Based on the results of the above sections, it is not unreasonable to expect that the first generation of EOR experiments may be able to go beyond simple detections of high redshift neutral hydrogen and distinguish between different theoretical reionization scenarios.

Several theoretical reionization models have been discussed in the literature (Santos et al. 2003; Zaldarriaga et al. 2004; Furlanetto et al. 2004a,b; Santos et al. 2005). Figure 5 shows the results of a simulation based on the example array configuration for redshift $z = 8$ and includes for comparison Furlanetto et al. (2004a,b) models for several power spectra with different reionization fractions. The solid black line and shaded gray regions are the same as in Figure 4, Column 2. It is immediately evident from the figure that the large changes in peak amplitude of the power spectra for these models would be ideal for constraining the ionization fraction.

4. EXPERIMENTAL CONSIDERATIONS

Radio observations in the meter bands are notoriously difficult. While this paper has focused on the theoretical sensitivity of first generation EOR observations, it is important to remember that there are many other observational difficulties which must be overcome by the experiments. In this section

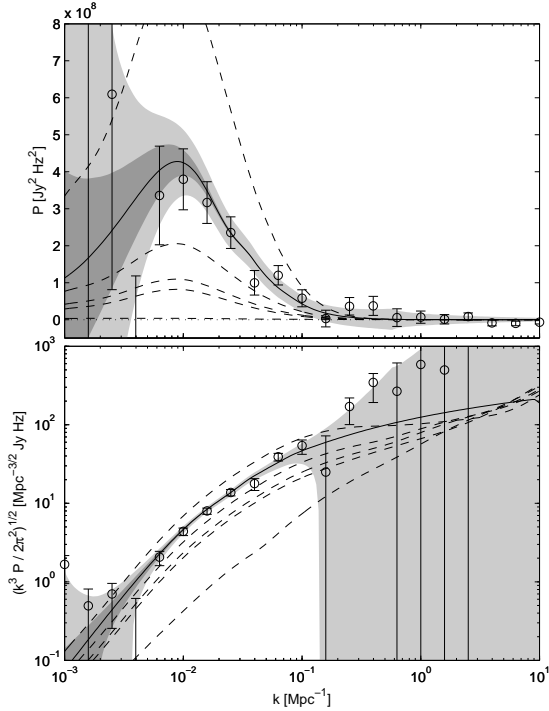


FIG. 5.— Same as Figure 4, Column 2 for redshift $z = 8$, but the data points show a simulated realization of the measured power spectrum. The error bars are the $1-\sigma$ uncertainties calculated from the thermal noise. The dashed lines are different values of the ionization fraction in the Furlanetto et al. (2004a,b) models and are, from top to bottom, $x_i = 0.51, 0.0$ (solid), $0.43, 0.38, 0.25$, and 0.13 . Note that the amplitude of the power spectrum for the fully neutral IGM is within those of the other ionization fractions. In general, the amplitudes of the model power spectra drop rapidly between $x_i = 0.0$ and 0.13 , and then slowly increase with ionization fraction as large bubbles increase the contrast.

we briefly describe some of the additional observational considerations.

The redshifted 21 cm radiation targeted by EOR experiments falls in the frequency range commonly used for television, FM radio, and satellite transmission. Both PAST and MWA have chosen very remote locations to get away from the radio communications which are now ubiquitous in many parts of the world, and all three experiments are developing advanced radio frequency interference (RFI) mitigation techniques.

Additionally, turbulence in the Earth’s ionosphere refracts low frequency radio waves. This acts much like atmospheric distortions at optical wavelengths, and must be corrected using techniques similar to wide-field adaptive optics.

After RFI and ionospheric distortions have been removed from the observations, there are still astrophysical foreground contaminants which are five orders of magnitude brighter than the EOR emission. Initial analysis suggested that these

foregrounds—which include synchrotron and free-free emission from the Galaxy, free-free emission from electrons in the IGM, and extended and point sources—were an insurmountable obstacle (Di Matteo et al. 2002; Oh & Mack 2003), but additional studies indicate that multi-frequency observations and statistical techniques should provide methods to separate the foregrounds from the EOR signal (Di Matteo et al. 2004; Zaldarriaga et al. 2004; Morales & Hewitt 2004; Santos et al. 2005).

Another concern is the instrumental effects related to galactic emission and imperfect instrumental calibration. Galactic synchrotron radiation dominates the sky at low radio frequencies and is responsible for the large system temperatures used in the fiducial observation. Additionally, the radiation is Faraday rotated by the interstellar medium and presents a bright, highly structured polarized emission pattern across the sky. This places very tight constraints on the precision of the instrumental polarization calibration.

All of these additional considerations should be manageable, but they complicate the analysis of the EOR power spectrum in actual observations. After removal or correction, each will produce a characteristic residual statistical signature in the observed data cylinder. Efforts are underway to assess the best techniques for addressing these contaminants and to estimate their residual statistical signatures.

5. CONCLUSION

Radio observations of the redshifted 21 cm emission during the epoch of reionization are capable of providing statistical measurements of the properties of neutral hydrogen at high redshift. These measurements can be carried out with the relatively small first-generation EOR instruments. Future larger arrays, such as the Square Kilometer Array, will be capable in principle of mapping individual features on the sky, and larger collecting areas should also allow high-precision measurements of the EOR power spectrum at higher redshifts, with important implications for fundamental cosmological measurements (Loeb & Zaldarriaga 2004).

In this paper, we have illustrated explicitly the fundamental uncertainties for a realistic experiment. This analysis provides a firm foundation to motivate continued development in this field.

Measurements of the reionization history are fundamental to understanding the evolution of the universe, and with properly designed experiments, these measurements are feasible and may be obtained in the very near future.

We would like to thank Matt McQuinn, Steve Furlanetto, and Matias Zaldarriaga for providing the theoretical reionization power spectra used in Section 3, and Brian Corey for supplying the photograph used in Figure 1. Support for this work was provided by NSF grant AST-0121164 and the MIT School of Science.

REFERENCES

- Alcock, C., & Paczynski, B. 1979, *Nature*, 281, 358
- Barkana, R., & Loeb, A. 2005a, *ApJ*, 624, L65
- Barkana, R., & Loeb, A. 2005b, *ApJ*, 626, 1
- Becker, R. H., et al. 2001, *AJ*, 122, 2850
- Bharadwaj, S., & Ali, S. S. 2005, *MNRAS*, 356, 1519
- Cen, R. 2003, *ApJ*, 591, 12
- Ciardi, B., & Madau, P. 2003, *ApJ*, 596, 1
- Di Matteo, T., Ciardi, B., & Miniati, F. 2004, *MNRAS*, 355, 1053
- Di Matteo, T., Perna, R., Abel, T., & Rees, M. J. 2002, *ApJ*, 564, 576
- Djorgovski, S. G., Castro, S., Stern, D., & Mahabal, A. A. 2001, *ApJ*, 560, L5
- Fan, X., et al. 2003, *AJ*, 125, 1649
- Furlanetto, S. R., & Briggs, F. H. 2004, *New Astronomy Review*, 48, 1039
- Furlanetto, S. R., Zaldarriaga, M., & Hernquist, L. 2004a, *ApJ*, 613, 16
- Furlanetto, S. R., Zaldarriaga, M., & Hernquist, L. 2004b, *ApJ*, 613, 1
- Haiman, Z., & Holder, G. P. 2003, *ApJ*, 595, 1

- Hogan, C. J., & Rees, M. J. 1979, MNRAS, 188, 791
- Iliev, I. T., Scannapieco, E., & Shapiro, P. R. 2005, ApJ, 624, 491
- Kaiser, N. 1987, MNRAS, 227, 1
- Kassim, N. E., Lazio, T. J. W., Ray, P. S., Crane, P. C., Hicks, B. C., Stewart, K. P., Cohen, A. S., & Lane, W. M. 2004, Planet. Space Sci., 52, 1343
- Kogut, A., et al. 2003, ApJS, 148, 161
- Loeb, A., & Zaldarriaga, M. 2004, Physical Review Letters, 92, 211301
- Madau, P., Meiksin, A., & Rees, M. J. 1997, ApJ, 475, 429
- Madau, P., Rees, M. J., Volonteri, M., Haardt, F., & Oh, S. P. 2004, ApJ, 604, 484
- Morales, M. F. 2005, ApJ, 619, 678
- Morales, M. F., & Hewitt, J. 2004, ApJ, 615, 7
- Oh, S. P., & Mack, K. J. 2003, MNRAS, 346, 871
- Pen, U. 2004, New Astronomy, 9, 417
- Pen, U. L., Wu, X. P., & Peterson, J. 2005, ChJAA, submitted
- Salah, J. E., Lonsdale, C. J., Oberoi, D., Cappallo, R. J., & Kasper, J. C. 2005, SPIE, in press
- Santos, M. G., Cooray, A., Haiman, Z., Knox, L., & Ma, C. 2003, ApJ, 598, 756
- Santos, M. G., Cooray, A., & Knox, L. 2005, ApJ, 625, 575
- Scott, D., & Rees, M. J. 1990, MNRAS, 247, 510
- Seljak, U., & Zaldarriaga, M. 1996, ApJ, 469, 437
- Shapiro, P. R., Giroux, M. L., & Babul, A. 1994, ApJ, 427, 25
- Sokasian, A., Abel, T., Hernquist, L., & Springel, V. 2003, MNRAS, 344, 607
- Somerville, R. S., Bullock, J. S., & Livio, M. 2003, ApJ, 593, 616
- Sunyaev, R. A., & Zeldovich, Y. B. 1972, A&A, 20, 189
- Tozzi, P., Madau, P., Meiksin, A., & Rees, M. J. 2000, ApJ, 528, 597
- Wyithe, J. S. B., & Loeb, A. 2004a, Nature, 432, 194
- Wyithe, J. S. B., & Loeb, A. 2004b, Nature, 427, 815
- Zaldarriaga, M., Furlanetto, S. R., & Hernquist, L. 2004, ApJ, 608, 622